

Heavy Meromyosin Molecules Extending More Than 50 nm above Adsorbing Electronegative Surfaces

Malin Persson,[†] Nuria Albet-Torres,[†] Leonid Ionov,[‡] Mark Sundberg,^{†,§} Fredrik Höök,^{||} Stefan Diez,[‡] Alf Månsson,[†] and Martina Balaz^{*,†,‡}

[†]School of Natural Sciences, The Linnaeus University SE-391 82 Kalmar, Sweden, [‡]Max-Planck-Institute of Molecular Cell Biology and Genetics, Pfotenhauerstrasse 108, 01307 Dresden, Germany, and

^{||}Chalmers University of Technology, Department of Applied Physics, SE-41296 Gothenburg, Sweden.

[§]Present address: Dilafor AB, Nobels väg 3, SE-171 77, Stockholm, Sweden. [‡]Present address: Lund University, Division of Solid State Physics, Box 188, 22100 Lund, Sweden.

Received January 27, 2010. Revised Manuscript Received March 8, 2010

In the *in vitro* motility assay, actin filaments are propelled by surface-adsorbed myosin motors, or rather, myosin motor fragments such as heavy meromyosin (HMM). Recently, efforts have been made to develop actomyosin powered nanodevices on the basis of this assay but such developments are hampered by limited understanding of the HMM adsorption geometry. Therefore, we here investigate the HMM adsorption geometries on trimethylchlorosilane-[TMCS-] derivatized hydrophobic surfaces and on hydrophilic negatively charged surfaces (SiO₂). The TMCS surface is of great relevance in fundamental studies of actomyosin and both surface substrates are important for the development of motor powered nanodevices. Whereas both the TMCS and SiO₂ surfaces were nearly saturated with HMM (incubation at 120 μg mL⁻¹) there was little actin binding on SiO₂ in the absence of ATP and no filament sliding in the presence of ATP. This contrasts with excellent actin-binding and motility on TMCS. Quartz crystal microbalance with dissipation (QCM-D) studies demonstrate a HMM layer with substantial protein mass up to 40 nm above the TMCS surface, considerably more than observed for myosin subfragment 1 (S1; 6 nm). Together with the excellent actin transportation on TMCS, this strongly suggests that HMM adsorbs to TMCS mainly via its most C-terminal tail part. Consistent with this idea, fluorescence interference contrast (FLIC) microscopy showed that actin filaments are held by HMM 38 ± 2 nm above the TMCS-surface with the catalytic site, on average, 20–30 nm above the surface. Viewed in a context with FLIC, QCM-D and TIRF results, the lack of actin motility and the limited actin binding on SiO₂ shows that HMM adsorbs largely via the actin-binding region on this surface with the C-terminal coiled-coil tails extending > 50 nm into solution. The results and new insights from this study are of value, not only for the development of motor powered nanodevices but also for the interpretation of fundamental biophysical studies of actomyosin function and for the understanding of surface–protein interactions in general.

Introduction

Muscle contraction results from ATP-driven, cyclic interactions between actin filaments and myosin II motors (henceforth myosin).¹ These motors are elongated asymmetric proteins, assembled via their predominantly coiled-coil tails into highly ordered thick filaments. During muscle contraction, flexible connections allow readjustments that enable the actin binding regions in the myosin motor domains to reach out 10–15 nm from the thick filament backbone and form force-producing actomyosin interactions.

In the *in vitro* motility assay (IVMA),^{1–3} myosin motors, or rather proteolytically prepared motor fragments, *e.g.*, heavy meromyosin (HMM), propel actin filaments while randomly adsorbed to artificial surfaces. In spite of widespread use of the IVMA, the mode of HMM adsorption has been characterized only to a limited degree.⁴ The great impact of surface-motor interactions is, however, evident from the dramatic differences in actin propelling capability when HMM is adsorbed to different

surface substrates.^{5–14} These differences have recently been exploited in developments toward motor driven lab-on-a-chip devices. Whereas the kinesin–microtubule system has been more frequently considered for such purposes actomyosin has certain potential advantages.^{15–20} In the previous studies,^{11–14,21} high

(5) Nicolau, D. V.; Solana, G.; Kekic, M.; Fulga, F.; Mahanivong, C.; Wright, J.; dos Remedios, C. *Langmuir* **2007**, *23*, 10846–10854.

(6) Warrick, H. M.; Simmons, R. M.; Finer, J. T.; Uyeda, T. Q.; Chu, S.; Spudich, J. A. *Methods Cell Biol.* **1993**, *39*, 1–21.

(7) Marston, S. J. *Muscle Res. Cell M.* **2003**, *24*, 149–156.

(8) Harada, Y.; Sakurada, K.; Aoki, T.; Thomas, D. D.; Yanagida, T. *J. Mol. Biol.* **1990**, *216*, 49–68.

(9) Albet-Torres, N.; O'Mahony, J.; Charlton, C.; Balaz, M.; Lisboa, P.; Aastrup, T.; Månsson, A.; Nicholls, I. A. *Langmuir* **2007**, *23*, 11147–11156.

(10) Sundberg, M.; Rosengren, J. P.; Bunk, R.; Lindahl, J.; Nicholls, I. A.; Tagerud, S.; Omling, P.; Montelius, L.; Månsson, A. *Anal. Biochem.* **2003**, *323*, 127–138.

(11) Suzuki, H.; Yamada, A.; Oiwa, K.; Nakayama, H.; Mashiko, S. *Biophys. J.* **1997**, *72*, 1997–2001.

(12) Nicolau, D. V.; Suzuki, H.; Mashiko, S.; Taguchi, T.; Yoshikawa, S. *Biophys. J.* **1999**, *77*, 1126–1134.

(13) Jaber, J. A.; Chase, P. B.; Schlenoff, J. B. *Nano Lett.* **2003**, *3*, 1505–1509.

(14) Sundberg, M.; Balaz, M.; Bunk, R.; Rosengren-Holmberg, J. P.; Montelius, L.; Nicholls, I. A.; Omling, P.; Tagerud, S.; Månsson, A. *Langmuir* **2006**, *22*, 7302–7312.

(15) Moorjani, S. G.; Jia, L.; Jackson, T. N.; Hancock, W. O. *Nano Lett.* **2003**, *3*, 633–637.

(16) Hess, H.; Clemmens, J.; Qin, D.; Howard, J.; Vogel, V. *Nano Lett.* **2001**, *1*, 235–239.

(17) Hess, H.; Bachand, G. D.; Vogel, V. *Chem.—Eur. J.* **2004**, *10*, 2110–2116.

(18) Goel, A.; Vogel, V. *Nat. Nanotechnol.* **2008**, *3*, 465–475.

*Address for correspondence. (M.B.) E-mail: martina.balaz@ftf.lth.se. Telephone: +46-46-2221472. Fax: +46-46-2223637. (A.M.) E-mail: alf.mansson@lnu.se. Telephone: +46-480-446243. Fax: +46-480-446262.

(1) Cooke, R. *Physiol. Rev.* **1997**, *77*, 671–697.

(2) Kron, S. J.; Spudich, J. A. *Proc. Natl. Acad. Sci. U.S.A.* **1986**, *83*, 6272–6276.

(3) Kron, S. J.; Toyoshima, Y. Y.; Uyeda, T. Q.; Spudich, J. A. *Methods Enzymol.* **1991**, *196*, 399–416.

(4) Månsson, A.; Balaz, M.; Albet-Torres, N.; Rosengren, K. J. *Front. Biosci.* **2008**, *13*, 5732–5754.

quality actin motility on moderately hydrophobic areas and the lack of motility on more negatively charged hydrophilic regions enabled control of the actin filament sliding along nanosized tracks. However, incomplete understanding of the HMM surface adsorption geometries that form the basis for the differences in function is an obstacle in the further exploitation of this approach for lab-on-a-chip devices.

Some insight of value in this connection was gained^{4,5,9,14} by combining IVMAs, ATPase assays and measurements of HMM mass adsorption on hydrophilic surfaces with large negative charge density (SiO₂ or glass) and on silanized hydrophobic surfaces (e.g., derivatized by trimethylchlorosilane, TMCS) with lower charge. Surprisingly, it was found that increased actin propelling capability on the latter surfaces was accompanied by a slightly reduced, rather than increased HMM surface density. The simplest model that accounts for this finding assumes HMM adsorption in two major configurations,^{4,9,14} one with good actin propelling capability, dominating on moderately hydrophobic surfaces and one with poor actin propelling capability, dominating on negatively charged hydrophilic surfaces (see further refs 20 and 22–24). The validity of this general model seems difficult to dispute but details of the HMM configurations and the thickness of the HMM surface layers are uncertain. Previous quartz crystal microbalance (QCM)⁹ studies only gave limited insight in this regard with estimates for the HMM layer height ranging from 10 to 70 nm. This is unsatisfactory since detailed height information is important for applications of actomyosin in nanotechnology. For instance, the optimal dimensions (height, width) of semiclosed nanoscale channels for spatial control of HMM driven actin motility are in a range (< 200 nm)^{21,25,26} where it is relevant, for the detailed design, to know whether the HMM layer height is 10 or 70 nm. Moreover, knowledge of this height is important in the design of surface patches for pickup or delivery of molecular cargoes^{27,28} since these patches need to reach the level where actin filaments are propelled by HMM.

We here take a multitechnique approach to investigate the above issues. Thus, for the first time in protein adsorption studies, quartz crystal microbalance with dissipation monitoring (QCM-D)^{29,30} is combined with fluorescence interference contrast (FLIC) microscopy^{31,32} and total internal reflection fluorescence (TIRF) spectroscopy (cf. refs 14 and 33). The combination of these techniques (principles described in Supporting Information)

allow detailed characterization of the dense HMM layer with substantial thickness and with a nonhomogeneous protein mass density distribution at different distances from the surface.

The data provide strong evidence for a dynamic HMM layer with a substantial fraction of the HMM mass extending to a height of 40 nm on TMCS and even more on SiO₂. Expanded versions of previous models^{4,9,14} for the HMM adsorption are proposed and the implications for nanotechnological applications are discussed as well as issues related to fundamental studies of motor function. Whereas the work is focused on interactions between the HMM molecules and artificial surfaces, the results also contribute to the general insight into surface–protein interactions, an issue that is still incompletely understood but of immense importance in different areas of biotechnology.^{34–36}

Some parts of the work have been presented in abstract form.³⁷

Materials and Methods

Chemicals. Tetramethylrhodamine phalloidin (RhPh) and Alexa-ATP (Alexa Fluor 647 2'-(or 3')-O-(N-(2-aminoethyl)-urethane), hexa(triethylammonium) salt) were purchased from Molecular Probes–Invitrogen (Eugene, OR). All other chemicals were of analytical grade and purchased from Merck (Darmstadt, Germany), Sigma-Aldrich (St. Louis, MO) or Fluka and Riedel-de Haën (Seelze, Germany).

Contact Angle Measurements and Surface Characterization by in Vitro Motility Assays. In order to verify adequate cleaning of pure SiO₂ surfaces by piranha solution (concentrated H₂SO₄ and 30% H₂O₂ in a 7:3 ratio), or proper derivatization with TMCS, advancing and receding contact angles were measured for water droplets on all surfaces.¹⁴ *Caution! Piranha solution is a highly corrosive acidic solution, which can react violently with organic materials. Do not store in closed container, and use appropriate safety precautions.* The surface properties were also verified with respect to the lack of HMM propelled actin motility on SiO₂ and high-quality motility (high velocity, > 70–80% of motile filaments) on TMCS derivatized surfaces (for details, see Supporting Information). In the following, TMCS-derivatized SiO₂ or glass surfaces will be referred to as TMCS-surfaces.

Preparation and Characterization of Proteins. Actin and myosin were purified from rabbit skeletal muscle,^{38,39} with myosin obtained from fast leg muscles (*musculus vastus lateralis* and *musculus tensor fasciae latae*),⁴⁰ back muscles (*musculus longissimus dorsi*) or, in some experiments, from *musculus psoas major*. Subsequent to myosin purification, heavy meromyosin (HMM) was prepared³ using TLCK-treated α-chymotrypsin in the presence of 2 mM Mg²⁺. Alternatively myosin Mg²⁺-subfragment 1 (S1) was prepared by papain digestion of myosin from *m. psoas major*, of the rabbit.³ In short, ammonium acetate buffer (200 mM, pH 7.2) containing 5 mM MgCl₂ and 1 mM DTT (dithiothreitol) was used for the digestion of 12 mg mL⁻¹ myosin with 0.27 units mL⁻¹ papain at 25 °C for 5 min. The reaction was stopped through addition of 20 μg mL⁻¹ E-64 followed by dilution of the protein solution with 2 volumes of a buffer containing 5 mM MgCl₂, 0.1 mM NaCHO₃, 0.1 mM EGTA (ethylene glycol bis(β-aminoethyl ether) N,N'-tetraacetic acid) and 2 mM DTT. The concentration of purified proteins was determined spectrophotometrically at 280 nm

(19) Bakewell, D. J. G.; Nicolau, D. V. *Aust. J. Chem.* **2007**, *60*, 314–332.

(20) Månsson, A.; Sundberg, M.; Bunk, R.; Balaz, M.; Nicholls, I. A.; Omling, P.; Tegenfeldt, J. O.; Tägerud, S.; Montelius, L. *IEEE Trans. Adv. Pack.* **2005**, *28*, 547–555.

(21) Bunk, R.; Sundberg, M.; Nicholls, I. A.; Omling, P.; Tägerud, S.; Månsson, A.; Montelius, L. *Nanotechnology* **2005**, *16*, 710–717.

(22) Diaz Banos, F. G.; Bordas, J.; Lowy, J.; Svensson, A. *Biophys. J.* **1996**, *71*, 576–589.

(23) Highsmith, S. *Biochemistry* **1990**, *29*, 10690–10694.

(24) Milligan, R. A. *Proc. Natl. Acad. Sci. U.S.A.* **1996**, *93*, 21–26.

(25) Sundberg, M.; Bunk, R.; Albet-Torres, N.; Kvennefors, A.; Persson, F.; Montelius, L.; Nicholls, I. A.; Ghattekar-Nilsson, S.; Omling, P.; Tägerud, S.; Månsson, A. *Langmuir* **2006**, *22*, 7286–7295.

(26) Vikhorev, P. G.; Vikhoreva, N. N.; Sundberg, M.; Balaz, M.; Albet-Torres, N.; Bunk, R.; Kvennefors, A.; Liljesson, K.; Nicholls, I. A.; Nilsson, L.; Omling, P.; Tägerud, S.; Montelius, L.; Månsson, A. *Langmuir* **2008**, *24*, 13509–13517.

(27) Dinu, C. Z.; Opitz, J.; Pompe, W.; Howard, J.; Mertig, M.; Diez, S. *Small* **2006**, *2*, 1090–1098.

(28) Brunner, C.; Wahnes, C.; Vogel, V. *Lab Chip* **2007**, *7*, 1263–1271.

(29) Hook, F.; Kasemo, B.; Nylander, T.; Fant, C.; Sott, K.; Elwing, H. *Anal. Chem.* **2001**, *73*, 5796–5804.

(30) Rodahl, M.; Hook, F.; Krozer, A.; Brzezinski, P.; Kasemo, B. *Rev. Sci. Instrum.* **1995**, *66*, 3924–3930.

(31) Braun, D.; Fromherz, P. *Appl. Phys. A: Mater.* **1997**, *65*, 341–348.

(32) Kerssemakers, J.; Howard, J.; Hess, H.; Diez, S. *Proc. Natl. Acad. Sci. U.S.A.* **2006**, *103*, 15812–15817.

(33) Balaz, M.; Sundberg, M.; Persson, M.; Kvassman, J.; Månsson, A. *Biochemistry* **2007**, *46*, 7233–7251.

(34) Kasemo, B. *Surf. Sci.* **2002**, *500*, 656–677.

(35) Gray, J. J. *Curr. Opin. Struct. Biol.* **2004**, *14*, 110–115.

(36) Nakanishi, K.; Sakiyama, T.; Imamura, K. *J. Biosci. Bioeng.* **2001**, *91*, 233–244.

(37) Balaz, M.; Persson, P.; Albet-Torres, N.; Sundberg, M.; Gunnarsson, A.; Höök, F.; Månsson, A. *Biophys. J.* **2009**, *96*, 495a.

(38) Pardee, J. D.; Spudich, J. A. *Methods Cell Biol.* **1982**, *24*, 271–289.

(39) Sata, M.; Sugiura, S.; Yamashita, H.; Momomura, S.; Serizawa, T. *Circ. Res.* **1993**, *73*, 696–704.

(40) Klinth, J.; Arner, A.; Månsson, A. *J. Muscle Res. Cell Motil.* **2003**, *24*, 15–32.

(myosin, HMM and S1) or 290 nm (actin) using extinction coefficients ($\text{dm}^3 \text{g}^{-1} \text{cm}^{-1}$) equal to those given earlier:³ 0.53 (myosin), 0.60 (HMM), 0.81 (S1), and 0.62 (actin). The quality of the protein preparations was verified by SDS-PAGE and by the fraction of motile filaments and sliding velocity in IVMAs (for details, see the Supporting Information).

HMM Surface Density from Depletion Studies. The amount of HMM adsorbed to SiO_2 or TMCS surfaces was determined from protein depletion of the incubation solution after incubation ($120 \mu\text{g mL}^{-1}$ HMM) of flow cells where both surfaces were either pure SiO_2 or TMCS-derivatized glass or SiO_2 .^{14,33} The amount of protein in the incubation solution was measured (using fluorescence spectroscopy) before and after a 2 min incubation period. The incubation period was terminated by extensive rinsing (10 cell volumes) to remove all nonadsorbed HMM from the flow cell^{14,33} and the entire effluent volume was collected for determination of the remaining amount of HMM. The difference between the amount of HMM in the incubation solution and this remaining amount was then divided by the total surface area of the flow cell to obtain the HMM surface density.

Quartz Crystal Microbalance with Dissipation (QCM-D) Studies. To assess HMM layer thickness and the dynamic nature of adsorbed HMM, a Qsense QCM-D (E4; Q-Sense AB, Västra Frölunda, Sweden) was employed. The silicon dioxide coated resonator chips were cleaned by a mixture of Milli-Q H_2O , H_2O_2 (30%) and NH_4OH (35%) at 5:1:1 volume proportions, for 10 min at 80 °C. A similar cleaning procedure was used prior to TMCS derivatization of the chips.⁹ All protein solutions were dissolved in Buffer A (10 mM MOPS pH 7.4, 2 mM MgCl_2 , 0.1 mM EGTA) with 15–20 mM KCl and 1 mM DTT and infused into the QCM-D flow cell (volume 40 μL ; active area 1.5 cm^2) using a flow rate of 600 $\mu\text{L min}^{-1}$. The QCM-D data were analyzed by a Voigt model representation using the software package Q-tools from Q-Sense AB according to principles described elsewhere.^{29,41}

Fluorescence Interference Contrast (FLIC) Microscopy: Actin Filaments. Highly polished single-crystal Si wafers with SiO_2 layers were subjected to steps of HF etching to produce a surface with terraces of different SiO_2 thicknesses.^{42,43} **Caution! HF is Highly toxic and corrosive even when diluted. It emits highly toxic HF gas. It irritates the skin and mucous membranes of the body. Handle with great care!** Subsequently, these wafers were either cleaned in piranha solution or cleaned in piranha solution followed by TMCS derivatization.^{10,14} The wafers were then characterized with regard to the SiO_2 thicknesses using an imaging ellipsometer (EP3, Nanofilm, Göttingen, Germany)³² Also contact angles were determined.

Flow cells were constructed by mounting the etched Si/ SiO_2 wafers on PEG-coated coverslips, using melted parafilm stripes as spacers. The grafting of poly(ethylene glycol) (PEG) self-assembled monolayer onto glass surfaces was performed as in^{44,45} with minor modifications (see Supporting Information). Wafers used for zero-height calibration of the FLIC-setup (see below) were immersed in 0.1 M NiCl_2 for at least 6 h prior to mounting in the flow cells. Here, as well as in subsequent steps, Ni^{2+} was included to allow adsorption of actin filaments directly on negatively charged surfaces.^{46,47}

In the zero-height calibration process, actin filaments were adsorbed directly onto the Si/ SiO_2 wafers, pretreated as above. The flow cell was then incubated with buffer A with 10 mM NiCl_2 (30 s) followed by RhPh labeled actin filaments (1–2 nM; 5 min). Subsequent to rinsing with buffer A with 30 mM KCl, and prior to

observation, the cell was incubated with an antifade solution (buffer A with 3 mg mL^{-1} glucose, 20 units mL^{-1} glucose oxidase and 868 units mL^{-1} catalase).

For observation of actin filaments bound to HMM or S1 (in the absence of ATP), the flow cells were first incubated for 2 min with 0.34 μM ($120 \mu\text{g mL}^{-1}$) HMM or 0.68 μM S1 in buffer A with 30 mM KCl and 1 mM DTT (Buffer A'), followed by rinsing with 2–4 volumes of buffer A'. Subsequently, the flow cells were incubated with RhPh labeled actin filaments (2–4 nM) and rinsed with 2 volumes of buffer A'. Finally, prior to observation at room temperature (20–23 °C), the flow cells were incubated with Buffer A' but with 10 mM DTT, supplemented with 3 mg mL^{-1} glucose, 20 units mL^{-1} glucose oxidase and 868 units mL^{-1} catalase.

To obtain sufficiently strong actin binding to HMM on SiO_2 , the FLIC studies of actin binding were performed using surfaces with a higher contact angle (30°) than in the rest of the experiments (<20°). That studies at this contact angle, by extrapolation, also should give insight into properties at lower contact angle, is suggested by findings⁹ that the HMM induced actin sliding velocity on a variety of negatively charged surfaces, increased nearly linearly with increased contact angle of these surfaces.

Images of actin filaments were acquired using an inverted fluorescence microscope (Eclipse TE300, Nikon, Tokyo, Japan) equipped with a Nikon 60x 1.20 NA water immersion objective, automatic shutter (Uniblitz VCM-D1, Vincent Associate, Rochester, NY), TRITC filter (Ex 540/25, DM 565 and BA 605/55), and a CCD camera (C9100–12, Hamamatsu, Hamamatsu City, Japan). A maximum number of three images was acquired on each position of the wafer, with an exposure time of 0.1 s. The average intensity of the 10 brightest pixels of each filament with a length > 3 μm was analyzed using a custom-made MatLab program (Matlab version 7.7.0.471, Mathworks, Natick, MA). Finally, the analyzed fluorescence intensities were plotted against the SiO_2 thicknesses and fitted by eq 1:

$$I(h_{\text{SiO}_2}) = I_1 + I_2 \left(\sin^2 \left(2\pi \frac{n_{\text{SiO}_2} \times h_{\text{SiO}_2} + n \times h}{\lambda_{\text{Ex}}} \right) \times \sin^2 \left(2\pi \frac{n_{\text{SiO}_2} \times h_{\text{SiO}_2} + n \times h}{\lambda_{\text{Em}}} \right) \right) \quad (1)$$

Here I_1 and I_2 represent the background intensity value and the intensity increase above this value at maximally constructive interference, respectively. Refractive indices for the buffer and SiO_2 layer were n ($= 1.333$) and n_{SiO_2} ($= 1.46$), respectively. The quantity h_{SiO_2} is the oxide thickness and h is the height of the fluorescent filament above the oxide surface. The excitation and emission wavelengths, λ_{Ex} and λ_{Em} , were taken as 540 and 605 nm, respectively as dictated by the use of a TRITC filter cube (see above). By fitting the data to eq 1, we obtained a height value, h , which represents the distance between the long axis of the actin filaments and the underlying TMCS surface. When the FLIC recordings were made, the HMM incubated surface had been rinsed with 6–10 volumes of HMM free solution, compared to 10 volumes in the HMM depletion studies.

FLIC Microscopy: Alexa ATP. Flow cells and surfaces as well as microscopy equipment was similar as in the FLIC microscopy with actin filaments. After preincubation of SiO_2 or TMCS derivatized FLIC surfaces with HMM ($120 \mu\text{g mL}^{-1}$) as described above, Alexa-ADP was locked to the active sites by incubation of 40 μM Alexa-ATP in the presence of 20 μM vanadate for 3 h. The surfaces were then washed with 4 volumes of Buffer A' followed by an antifade solution (Buffer A', 10 mM DTT, 2.5 mM 3,4-dihydroxybenzoic acid, 1 mM Trolox and 50 nM protocatechuate 3,4-dioxygenase) before observation in the microscope using a Cy5 filter cube (Ex 620/60, DM 660 and BA 700/75). Control experiments were performed to verify that the antibleach mixture did not affect the fraction of motile filaments or the sliding velocity in IVMAs.

(41) Asberg, P.; Bjork, P.; Hook, F.; Inngan, O. *Langmuir* **2005**, *21*, 7292–7298.

(42) Lambacher, A.; Fromherz, P. *Appl. Phys. A: Mater.* **1996**, *63*, 207–216.

(43) Ionov, L.; Sapra, S.; Snytnska, A.; Rogach, A. L.; Stamm, M.; Diez, S. *Adv. Mater.* **2006**, *18*, 1453.

(44) Papra, A.; Gadegaard, N.; Larsen, N. B. *Langmuir* **2001**, *17*, 1457–1460.

(45) van den Heuvel, M. G. L.; Butcher, C. T.; Lemay, S. G.; Diez, S.; Dekker, C. *Nano Lett.* **2005**, *5*, 235–241.

(46) Pestre, D.; Pietrement, O.; Zozime, A.; Le Cam, E. *Biopolymers* **2005**, *77*, 53–62.

(47) Hansma, H. G.; Laney, D. E. *Biophys. J.* **1996**, *70*, 1933–1939.

TIRF Spectroscopy: General Aspects. UV fused silica slides (SiO₂, TIRF Technologies, Inc., Harrisburg, PA), used for total internal reflection fluorescence (TIRF) measurements were either cleaned in piranha solution or precleaned in piranha solution and silanized by liquid deposition of TMCS.^{10,14} All TIRF spectroscopy studies were performed using a total internal reflection fluorescence (TIRF) flow system (BioElectroSpec Inc., Harrisburg, PA) integrated into a SPEX Fluorolog-3–22 spectrofluorometer (Jobin Yvon Instruments, Edison, NJ). Controlled fluid injection into the TRIF cell was achieved using a syringe pump 50300 (Kloehn, Las Vegas, NV). The DataMax software (version 2.10, Jobin Yvon) was employed for data analysis.

TIRF Spectroscopy Studies of HMM Intrinsic Fluorescence. For the study of HMM intrinsic fluorescence the incident angle for the excitation light ($\lambda = 280$ nm; slit size 2 nm) was generally set to 69.4°, corresponding to a penetration depth of 73 nm (Supporting Information, eq 1). Emission was monitored at 332 nm (slit size 6 nm) at an acquisition rate of 1 s⁻¹. The TIRF flow cell (volume 34 μ L; height 100 μ m; active area 3.4 cm²) was incubated with HMM (120 μ g mL⁻¹) in a buffer (Buffer B; flow rate of 313 μ L min⁻¹) of the following composition: 25 mM imidazole–HCl (pH 7.4), 4 mM MgCl₂, 25 mM KCl, 1 mM EGTA, and 1 mM DTT. In one set of experiments, we studied effects of altered penetration depth of the evanescent wave on the HMM intrinsic fluorescence. Following HMM adsorption and subsequent rinsing, to remove HMM in the bulk solution, a given sequence of changes in the penetration depth was achieved by varying the incident angle for the excitation beam. The intensity of the intrinsic HMM fluorescence emission was normalized to that at a penetration depth of 59 nm and a ratio between TMCS and SiO₂ was obtained for each penetration depth. (see Supporting Information for details).

Alexa-ATP: TIRF Spectroscopy. Unless otherwise stated, the incident angle for the excitation light at ($\lambda = 649$ nm) was 69.4°, corresponding to an evanescent wave penetration depth of 170 nm. The binding and subsequent turnover of Alexa-ATP was studied as described previously³³ (Supporting Information for details). Following HMM incubation (120 μ g mL⁻¹; 2 min), Alexa-ATP (3–5 μ M) was infused. Upon saturation of the HMM active sites with Alexa-nucleotide, an Alexa-ATP free buffer solution with regular ATP was rapidly infused. The resulting fluorescence decay ($I_N(t)$; normalized to initial fluorescence intensity) was fitted by a sum of a three exponentials with amplitudes A_1 , A_2 , and A_3 and rate constant k_1 , k_2 , and k_3 as follows:

$$I_N(t) = A_1e^{-k_1t} + A_2e^{-k_2t} + A_3e^{-k_3t} \quad (2)$$

Here, t is the time after onset of rinsing with Alexa-ATP free solution. The quantity $(1 - (A_1 + A_2 + A_3))$ approximates the contribution from Alexa-ATP in bulk solution, to the fluorescence intensity during the peak of the Alexa-ATP transient, *i.e.*, before rinsing. To avoid interference from the decay in this bulk signal, the fitting to eq 2 was limited to times 3–5 s after the onset of this rinsing step (2–4 s after onset of fluorescence decay). The HMM density (from intrinsic protein fluorescence) on SiO₂ was higher than on TMCS throughout the Alexa-ATP experiments in spite of increased desorption from SiO₂ upon rinsing (Supporting Information Figure 3B).

Statistical Analysis. Nonlinear regression and statistical analyses were performed using Graph Pad Prism software (version 4.0 or 5.0 GraphPad Software, San Diego, CA). Data are given as mean \pm standard error of the mean (SEM).

Results

General Data: HMM Density and HMM Function on SiO₂ and TMCS. The SiO₂ surfaces had advancing contact angle $< 20^\circ$ (unless otherwise stated below) compared to $\sim 70^\circ$ for TMCS surfaces. No HMM induced actin motility was observed

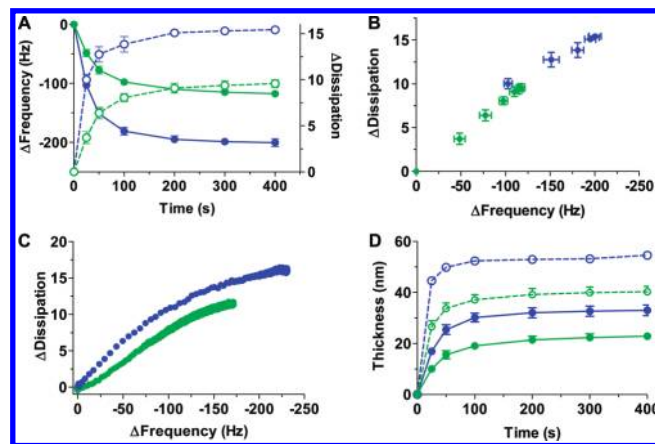


Figure 1. HMM adsorption data recorded using quartz crystal microbalance with dissipation monitoring (QCM-D). (A) Changes in resonance frequency (Δf , filled symbols left vertical axis) and dissipation ($\Delta D/10^{-6}$; open symbols, right vertical axis) for TMCS (green) and SiO₂ (blue) early after incubation with HMM (120 μ g mL⁻¹). The data (mean \pm SEM) were obtained in 4–5 different experiments by driving the QCM chip at 15 MHz (3 times the resonance frequency). Same color codes in B–D as in panel A. (B) Quantity ΔD plotted against Δf for the data in part A. (C) Plots of ΔD vs Δf for one given experiment with prolonged HMM incubation. (D) Thickness of the HMM layers on SiO₂ and TMCS, calculated using a Voigt model assuming high (filled symbols and filled lines) or low shear modulus (open symbols and dashed lines). The model made use of data in part A and similar data obtained by driving the QCM chip at 7 and 13 times the fundamental frequency. $T = 22$ – 25 °C.

on SiO₂ whereas there was high quality motility (high fraction of motile filaments and high velocity) on TMCS. The degree of actin filament binding to HMM was negligible on SiO₂ in the presence of ATP and also consistently lower on SiO₂ than on TMCS in the absence of ATP. In cases where the piranha cleaning had been particularly effective the contact angle of water droplets was less than 10° and in these cases there was generally no actin binding to HMM in the absence of ATP. TIRF spectroscopy data demonstrated 50% higher increase in protein fluorescence on SiO₂ than on TMCS upon HMM incubation, indicating greater initial HMM adsorption on SiO₂. Extensive rinsing of the TIRF flow cell caused some desorption from SiO₂ but very little desorption from TMCS, bringing the HMM density on TMCS and SiO₂ quite close to each other. Consistent with these findings, the HMM surface density, measured from HMM depletion of the incubation solution (involving several rinsing steps), suggested no significant difference in HMM density: 6587 ± 369 molecules μm^{-2} ($n = 8$) on SiO₂ and 6519 ± 319 molecules μm^{-2} ($n = 9$) on TMCS. Further details of the above results are given in the Supporting Information.

QCM-D Studies Suggest Thicker HMM Layer on SiO₂ Than on TMCS. The changes in resonance frequency (Δf) and energy dissipation, ΔD in QCM-D studies provide information about mass, solvent content, thickness and the viscoelastic properties of adsorbed protein layers.^{29,48,49} The results from five different QCM-D experiments (Figure 1A) showed greater reduction in Δf , for SiO₂ than for TMCS surfaces upon incubation with HMM. Similar effects were observed when driving the

(48) Bingen, P.; Wang, G.; Steinmetz, N. F.; Rodahl, M.; Richter, R. P. *Anal. Chem.* **2008**, *80*, 8880–8890.

(49) Hook, F.; Voros, J.; Rodahl, M.; Kurrat, R.; Boni, P.; Ramsden, J. J.; Textor, M.; Spencer, N. D.; Tengvall, P.; Gold, J.; Kasemo, B. *Colloids Surf., B* **2002**, *24*, 155–170.

QCM-oscillation at 3, 5, 7, and 13 times the fundamental frequency (f_0).

The larger Δf values for SiO₂ compared to TMCS surfaces were accompanied by larger changes in dissipation (ΔD ; Figure 1A). Similar results were found at the different multiplicities of f_0 . The time course of the changes in Δf and ΔD differed between TMCS and SiO₂. This is illustrated in Figure 1B indicating a slightly higher slope of the $\Delta D - \Delta f$ relation for SiO₂ than for TMCS at $\Delta f < 100$ Hz during the HMM adsorption phase. The higher initial slope is more evident from the individual experiment in Figure 1C where the ΔD is plotted versus Δf for the entire adsorption process, consistent with a less rigid protein film on SiO₂.

Analysis of the QCM-D data using a Voigt model²⁹ suggested a time course for the increase in HMM layer thickness on TMCS and SiO₂ as illustrated in Figure 1D (full symbols and lines). After 2 min, the thickness was 21 ± 1.5 nm ($n = 5$) and 32 ± 2 nm ($n = 5$) on TMCS and SiO₂, respectively. These thickness values correspond to total coupled mass (HMM and hydrodynamically coupled solvent) of 2200 and 3400 ng cm⁻² on TMCS and SiO₂, respectively on the basis of the density of protein (1400 kg m⁻³) and solvent (1000 kg m⁻³) and the number of HMM molecules per surface area 2 min after adsorption. Out of the total adsorbed mass only 380 ng (17%) on TMCS and 440 ng (13%) on SiO₂, were attributed to HMM.

The above thickness estimates refer to a film representation characterized by a high shear modulus ($> 0.5 \times 10^4$ Pa), previously shown to yield thickness estimates for DNA as well as globular and flexible proteins in good agreement with *e.g.*, surface plasmon resonance and ellipsometry data.^{29,50} In the Voigt model, the adsorbed proteins are represented by a single homogeneous film characterized by four parameters: thickness, density, shear viscosity, and shear elastic modulus. Within the small density interval between that of water (1000 kg m⁻³) and protein (1400 kg m⁻³) the thickness and density cannot be accurately separated. Rather, the product of the two (*i.e.*, the coupled mass) remains conserved. Hence, if only a fraction of a monolayer of proteins is adsorbed, the determined effective thickness will, to a first approximation, scale with coupled mass. However, not all solvent contained between the adsorbed proteins contributes to this coupled mass. Therefore, one should regard the estimated thicknesses, obtained under the constraint of a high shear modulus, as the minimum values. Moreover, for flexible films, essentially equally good fits can generally be obtained if the shear modulus is forced to be low ($< 0.5 \times 10^4$ Pa). For this representation, HMM layer thickness of 39 ± 2 nm and 53 ± 1 nm ($n = 5$) were obtained on TMCS and SiO₂, respectively (open symbols and dashed lines in Figure 1D). This is tentatively attributed to model settings forced to predominantly represent the flexible properties of the film extending further out from the surface. These higher thickness values are in good agreement with the results below (Figure 2) demonstrating actin binding of HMM up to 40 nm from the surface on TMCS and more than 50 nm from the surface on SiO₂ (see also Discussion).

If the surface was incubated with myosin subfragment 1 (S1), the $\Delta D/\Delta f$ ratio after 2 min was considerably lower than with HMM. Modeling as above, using the high shear representation, gave an S1 layer thickness of 5.7–7.2 nm ($n = 2$) on TMCS and 5.2–7.1 nm ($n = 3$) on SiO₂. The low shear representation gave inconsistent modeling results.

FLIC Microscopy: Higher HMM Layer on SiO₂ Than on TMCS but HMM Catalytic Sites Closer to the Surface on SiO₂. The FLIC system was first calibrated by observing fluorescent actin filaments (Figure 2A) adsorbed directly onto a

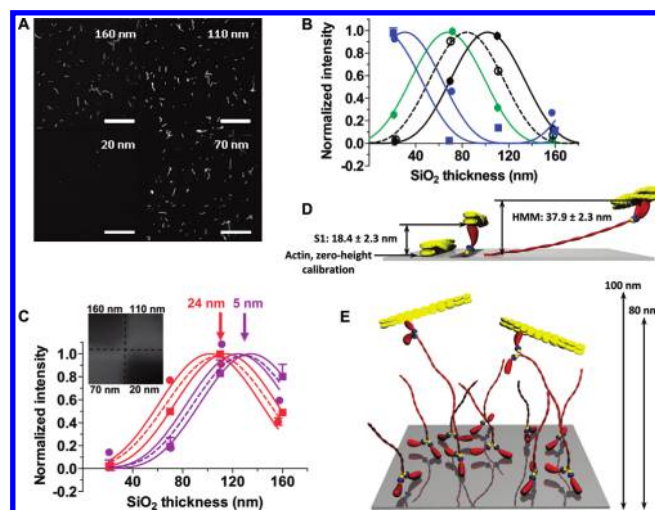


Figure 2. Fluorescence interference contrast (FLIC) microscopy data showing intensity vs height of underlying SiO₂ layer and fits of eq 1 (lines). (A) Fluorescence micrographs with actin filaments adsorbed directly to SiO₂ surface (used for “zero height calibration”) with heights of the SiO₂ layer indicated in the figure. Scale bar: 20 μ m. (B) FLIC data for actin filaments adsorbed directly to surface (filled black symbols and full line), bound to subfragment 1 (open black symbols and dashed line) or to HMM (filled green symbols and line) on TMCS or to HMM on SiO₂ (2 surfaces, different blue symbols and lines). Each data point represents average of 210–632 and 105–432 filaments on 2 TMCS and 2 SiO₂ surfaces, respectively. (C) Data for Alexa-nucleotide locked (in the presence of vanadate) to catalytic sites of HMM on TMCS (2 surfaces, different red symbols and lines) and on SiO₂ (2 surfaces, different purple symbols and lines). Each data point represents average intensity values measured over areas $> 10 \times 10 \mu$ m² from one given fluorescence micrograph, similar to that in the inset, showing the intersection point of all SiO₂ terraces. Arrows point to SiO₂-heights for maximum intensity predicted from eq 1 for distances of 24 and 5 nm between Alexa-nucleotide and the surface. Dashed lines represent a sum of three terms like those in eq 1 (Supporting Information, eq 8) fitted to all the data on TMCS (red) or SiO₂ (purple) on the assumption of a distribution with different fractions of the catalytic sites at different heights above the surface. For details, see text and the Supporting Information. Inset: Fluorescence micrograph of Alexa-nucleotide bound to HMM on TMCS at the intersection point between the four SiO₂ terraces of different heights, (in nm, indicated by numbers). Image subjected to histogram-stretching for intensity enhancement. (D) Summary of FLIC results illustrating actin filaments (yellow) adsorbed directly to a surface or bound to S1 or HMM on a TMCS surface. (E) Interpretation of FLIC data for HMM adsorption on SiO₂. If applicable but not shown, the error bars (SEM) were smaller than the size of the symbols. Temperature: 20–23 $^{\circ}$ C.

Si/SiO₂ surface via positively charged divalent cations (Ni²⁺). Fluorescence intensity data are shown in Figure 2B (filled black circles) for one of the calibration surfaces, together with the fitted FLIC curve (eq 1; full black line). This fit gave an average reference height to be subtracted from the height data for actin filaments bound to myosin motor fragments and for Alexa-nucleotide locked to the active site of HMM (after taking actin filament width into account).

Experimental data for actin filament binding to S1 and HMM are also illustrated in Figure 2B. It can be seen that the curve for actin binding to S1 (black open symbols, dashed lines) and HMM (green symbols and line) on TMCS are shifted to the left compared to the calibration data (black filled symbols and full line) and, as expected, the shift is larger for HMM than for S1. Subtraction of the average calibration value from the head-surface distance in fits of eq 1 (cf. ref 32) suggests that the

(50) Larsson, C.; Rodahl, M.; Hook, F. *Anal. Chem.* **2003**, *75*, 5080–5087.

HMM and S1 molecules hold the actin filaments 37.9 ± 2.3 nm and 18.4 ± 2.3 nm, respectively above the TMCS surface. The standard error values in these estimates were calculated as described in the Supporting Information.

A sufficient number of strongly bound actin filaments were possible to study also on SiO₂ surfaces if these were subjected to less aggressive piranha cleaning than in the majority of the experiments. In spite of the slightly higher contact angle on such surfaces (advancing contact angle, 30°) the data provide insight into the HMM adsorption mechanism also at the lowest contact angles (see Materials and Methods). Because of greater variability than in the other experiments, the FLIC curves of both individual experiments for actin binding to HMM on SiO₂ are shown (blue symbols and curves in Figure 2B). It can be seen that the curves are shifted further to the left than for actin binding on TMCS. Fits of eq 1 suggest heights of 83 and 105 nm above the SiO₂ surface in the two experiments.

The FLIC intensity values upon locking Alexa-nucleotide to the active site of HMM on two different TMCS surfaces are illustrated in Figure 2C (red). Experimental raw data for this case are exemplified by the fluorescence micrograph in Figure 2C (inset). Fits of eq 1 (filled red lines) suggest average heights of the catalytic sites above the TMCS surfaces of 18 and 30 nm in the two different experiments. As is also seen in Figure 2C, the FLIC curves for Alexa-nucleotide binding suggest that the catalytic sites are closer to the SiO₂ (purple) than to the TMCS surface (red). The distance to the SiO₂ surface is in the range 0–10 nm according to fits to eq 1 (filled purple lines).

It is reasonable to presume that the catalytic sites of HMM are not all located at the same height above the surface. Rather, there is a distribution with catalytic sites found at different heights, ranging from direct contact with the surface to >38 nm (on TMCS) or >80 nm (on SiO₂) above the surface (Figure 2B). We therefore tested whether the data in Figure 2C could be reasonably fitted by such a distribution of heights. For this purpose we assumed just three heights occurring with different probabilities as a simplified approximation of a continuous distribution. Thus, the sum of three equations similar to eq 1 was fitted to data from both experiments on TMCS and SiO₂ (dashed line in Figure 2C) with the assumption of different fractions of the catalytic sites being at three different heights (for details, see Supporting Information). As illustrated in Figure 2C (dashed lines) the data on TMCS for Alexa-nucleotide are reasonably well fitted ($r^2 \approx 0.95$) by a distribution with 30%, 60%, and 11% of the catalytic sites 10, 28, and 38 nm above the surface, respectively. It can also be seen in Figure 2C that the data on SiO₂ for Alexa-nucleotide are well fitted by a distribution with 29%, 70%, and 1% of the catalytic sites 4 nm, 5 and 90 nm above the surface, respectively. Indeed, this suggests that the data on SiO₂ are well accounted for by just two populations of HMM molecules: one dominant population (99% of all molecules) with the heads within 5 nm from the surface and one small population (1%) with heads at heights up to approximately 100 nm above the surface.

In summary, this section shows that HMM holds actin filaments almost 40 nm above the TMCS surface (Figure 2D), considerably higher than with S1 and higher than the average position of the catalytic site. On SiO₂ surfaces (Figure 2E), HMM holds the actin filaments >80 nm from the surface whereas a vast majority of the active sites are within approximately 5 nm from the surface. Finally, the Alexa-nucleotide studies are consistent with a continuous distribution of heights of the catalytic sites above the TMCS surface whereas the data for SiO₂ are well accounted for by two discrete populations with the catalytic sites

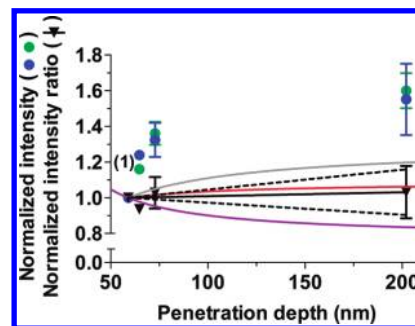


Figure 3. Intrinsic HMM fluorescence at different penetration depths as calculated from the incident angle for the excitation light. Intensities (emission at 332 nm) normalized to that at a penetration depth of 59 nm for 7 HMM incubated SiO₂ surfaces and 6 TMCS surfaces except for one of the penetration depths (1 experiment as indicated in parentheses). Circles refer to experimental data (SiO₂, blue; TMCS, green) and triangles (black) indicate the ratio between these TMCS and SiO₂ values. Error bars refer to SEM, calculated by error propagation for the ratios. The lines represent theoretical relations (eq 3) for 5 nm higher (red), 15 nm higher (gray), or 15 nm lower (purple) head-surface distance on TMCS than on SiO₂. The full black line represents a regression line forced through the point at 59 nm penetration depth. Dashed black lines represent 95% confidence interval in the regression analysis. $T = 25 \pm 0.5$ °C.

within 5 nm from the surface (99%) and 80–100 nm from the surface (1%), respectively.

TIRF Spectroscopy of HMM Intrinsic Fluorescence Suggest Similar Head–Surface Distance on TMCS and SiO₂.

For further insight into differences in mode of adsorption between TMCS and SiO₂ we studied protein fluorescence upon TIRF excitation using evanescent waves of different penetration depths (d_p). Since the HMM intrinsic fluorescence originates only in the head and neck domains, with all tryptophans and tyrosines, height differences of these regions between TMCS and SiO₂ should be detectable. A relevant quantity to monitor is the intensity ratio (Figure 3, triangles) between HMM fluorescence on TMCS (Figure 3, green) and SiO₂ (Figure 3, blue) at different evanescent wave penetration depths. Theoretically (Supporting Information), this ratio ($R(d_p)$) should be related to the height difference between the myosin head-necks on TMCS and SiO₂ ($h^{\text{TMCS}} - h^{\text{SiO}_2}$) according to:

$$R(d_p) = \exp \left(- (h^{\text{TMCS}} - h^{\text{SiO}_2}) \left(\frac{1}{d_p} - \frac{1}{d_p^{\text{ref}}} \right) \right) \quad (3)$$

where d_p^{ref} is a reference penetration depth (here, 59 nm). The theoretical relation (eq 3) is plotted against d_p in Figure 3 on the assumption of 5 nm higher (red), 15 nm higher (gray), or 15 nm lower (purple) average head–surface distance on TMCS than on SiO₂. The data (triangles) indicate a small difference between TMCS and SiO₂ with the 95% confidence interval in the regression analysis within the theoretical relations for ± 15 nm height difference.

Time Course of Alexa-ATP TIRF Transients Consistent with Immobilization of Larger Fraction of HMM Heads on SiO₂ Than on TMCS. Fluorescent Alexa-ATP³³ was added to TIRF flow cells, preincubated with 120 $\mu\text{g mL}^{-1}$ HMM (Figure 4). Different fluorescence amplitudes were observed on TMCS and SiO₂ upon binding of Alexa-ATP to HMM but, importantly (Supporting Information), this is due to different degrees of fluorescence quenching and not to different active site concentrations.

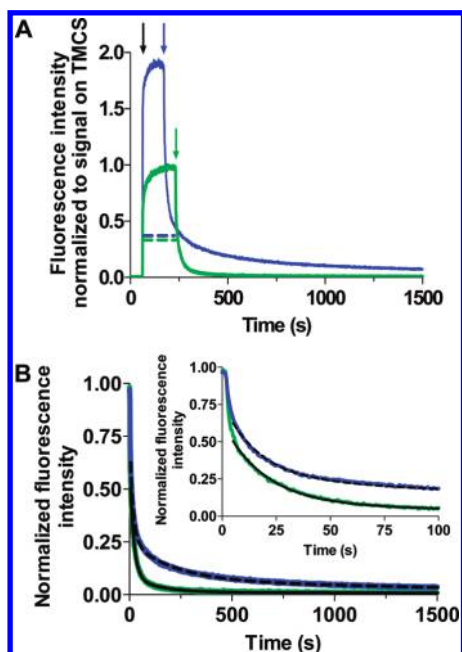


Figure 4. Total internal reflection fluorescence (TIRF) transients due to Alexa-ATP incubations of TIRF flow cell subsequent to HMM adsorption. (A) Fluorescence intensity time courses for TIRF slides (SiO₂, blue; TMCS, green) incubated with 3 μ M Alexa-ATP. Data normalized to peak value of the fluorescence signal on TMCS. The TMCS and SiO₂ surfaces were incubated with 120 μ g mL⁻¹ HMM, prior to incubation with Alexa-ATP (time 60 s; black arrow). After attainment of a steady fluorescence level, the Alexa-ATP solution was quickly exchanged for fluorophore free solution with regular ATP (at blue arrow on SiO₂ and at green arrow on TMCS). Straight dashed lines indicate fluorescence intensity levels attributed to bulk and nonspecific binding of Alexa-ATP to HMM on TMCS (green) and SiO₂ (blue). (B) The time course for the fluorescence decay from part A replotted (normalized to the maximum fluorescence intensity in each given experiment) with the same color code as in part A. Inset shows the first 100 s of the decaying fluorescence signal. Triple-exponential functions fitted by nonlinear regression shown as dashed black line for SiO₂ ($y = 0.51e^{-0.060t} + 0.18e^{-0.0049t} + 0.074e^{-0.00050t}$ and $r^2 = 0.998$) and full black line for TMCS ($y = 0.54e^{-0.052t} + 0.081e^{-0.0079t} + 0.012e^{-0.00029t}$ and $r^2 = 0.996$). $T = 25 \pm 0.5$ °C. The amplitudes of the exponential processes sum up to 0.764 and 0.634 for SiO₂ and TMCS, respectively. The difference from 1 is attributed to bulk contributions and nonspecific binding. Fit limited to times > 6 s.

After the Alexa-ATP fluorescence transients had reached their maximal values (second arrows Figure 4A), the fluorescent bulk solution was exchanged for a solution containing regular ATP.³³ The resulting decay of the fluorescence signal is shown in Figure 4B together with fits of triple exponential functions. Table 1 summarizes the results from 5 experiments with different combinations of HMM preparations and surface batches. Whereas the fastest (k_1) and slowest (k_3) rate constants were similar on TMCS and SiO₂, the intermediate rate constant (k_2) was lower on SiO₂. Most importantly, however, the amplitudes of the two slowest phases (A_2 and A_3) made up a considerably higher fraction of the total amplitude ($A_1 + A_2 + A_3$) on SiO₂ (36%), than on TMCS (16%). In contrast to the difference between the time courses on TMCS and SiO₂, a reduction in temperature from 25 to 15 °C reduced the rate constants of all the exponential processes (Supporting Information Table 1). Finally, three phases in the decay of the Alexa-ATP transients were observed also in rabbit *psaos* muscle (Supporting Information Table 2) and the

difference between TMCS and SiO₂ was similar as for the fast leg muscle. This is important since the *psaos* muscle is dominated by one single myosin isoform (IId/IIx).⁵¹

The results are consistent with the idea that a larger fraction of the HMM molecules on SiO₂ than on TMCS exhibits a slow ATP turnover. This, in turn, fits with the idea that they are immobilized to the surface to larger degree via their head parts, in agreement with the results in Figure 2C.

Discussion

General Discussion. The present experimental design allows direct comparison to earlier studies of HMM function on TMCS and pure SiO₂/glass surfaces.^{9,14,25,33} The similarity to conditions in the earlier studies was verified by contact angle measurements, *in vitro* motility assays and HMM adsorption studies. Thus, in spite of only limited actin binding to HMM in the absence of ATP and no motility on SiO₂, the HMM density on this surface was as high as on TMCS. On both surfaces, the HMM density was close to jamming conditions ($\sim 6500 \mu\text{m}^{-2}$; 56% of full surface coverage, 11 500 μm^{-2}) in a random sequential adsorption model⁵² for spherical proteins. This corresponds to a footprint for each HMM molecule of 159 nm² with a nearest neighbor distance < 7 nm.

Comparison between QCM-D and FLIC Results. The FLIC data suggest that HMM holds the actin filaments 38 nm above the TMCS surface. In contrast, the conventional method to analyze QCM-D data (high shear representation) suggests a HMM layer thickness of 21 nm, indicating that the largest fraction of the HMM and coupled solvent mass can be found below this height. However, an alternative film representation (low shear), that also gave good fits in QCM-D based modeling, suggested a height of the HMM layer of 39 nm, in good agreement with the FLIC results. We attribute the two representations to sensitivity of the Voigt model to film inhomogeneity. For example, if the protein density is higher close to the substrate, gradually decreasing values of film density, shear modulus and viscosity would be a more accurate representation. Such inhomogeneity is consistent with the FLIC studies of Alexa-nucleotide (dashed lines in Figure 2C) but implementation of such a model for the QCM-D data is beyond the scope of the present work.

The FLIC and QCM-D studies suggest that the actin binding HMM molecules on TMCS are among those that reach furthest above the surface. This accords with an expected difficulty for actin filaments, with persistence length of about 10 μm ,⁵³ to penetrate a crowded HMM layer. It also accords with the FLIC results with Alexa-nucleotide suggesting that a majority of the HMM catalytic sites are closer to the TMCS surface than the HMM-held actin filaments.

For SiO₂, the high shear and low shear representations of the QCM-D data suggested HMM layer heights of 31 and 55 nm, respectively. As the Alexa-nucleotide FLIC experiments suggest that a majority of the catalytic sites are within 5 nm from the SiO₂ surface the large height values from the QCM-D analysis must be attributed mainly to HMM tails extending into solution.

It was of interest to also consider data with myosin subfragment-1 since the myosin heads, in this case, are necessarily adsorbed directly to the surface. The FLIC studies suggested that S1 holds actin filaments 18 nm above the surface on TMCS, in

(51) Hamalainen, N.; Pette, D. *J. Histochem. Cytochem.* **1993**, *41*, 733–743.

(52) Valimaa, L.; Pettersson, K.; Rosenberg, J.; Karp, M.; Lovgren, T. *Anal. Biochem.* **2004**, *331*, 376–384.

(53) Vikhoreva, P. G.; Vikhoreva, N. N.; Mansson, A. *Biophys. J.* **2008**, *95*, 5809–5819.

Table 1. Results of Triple Exponential Fits to Decaying Phase of Alexa-ATP TIRF Transient, Where Data (Mean \pm SEM) Are for HMM Purified from Fast Leg Muscles of the Rabbit ($T = 25 \pm 0.5^\circ\text{C}$)

	k_1 (s^{-1})	k_2 (s^{-1})	k_3 (s^{-1})	A_1 (%) ^b	A_2 (%) ^b	A_3 (%) ^b
<i>TMCS Surface</i>						
fast leg muscle ($n = 4$) ^a	0.051 ± 0.002	0.0078 ± 0.0005	0.00041 ± 0.00008	84 ± 0.4	13 ± 0.4	2.8 ± 0.4
<i>SiO₂ Surface</i>						
fast leg muscle ($n = 4$) ^a	0.057 ± 0.003 (n.s.) ^d	0.0048 ± 0.00009 ^c	0.00053 ± 0.00003 ^d	64 ± 1.1 ^c	25 ± 0.6 ^c	11 ± 0.8 ^c

^aSEM obtained from variability between experiments. ^bAmplitudes normalized to sum ($A_1 + A_2 + A_3$). ^cSignificant difference between data on TMCS and SiO₂ ($p < 0.001$). ^dn.s.: not significant (paired t tests).

accordance with the view that S1 (approximate length 16–20 nm) adsorbs at the papain-cleavage site at the C-terminal and then extends by almost its entire length above the surface. In contrast to the FLIC data, the QCM-D results for both TMCS and SiO₂ indicate an S1-layer thickness of about 6 nm. The discrepancy may be resolved in an analogous way as suggested for HMM, *i.e.*, by attributing actin binding to a small fraction of the S1-units that extend furthest above the surface.

Alexa-ATP Transients: Methodological Issues. The idea that all exponential processes in the Alexa-ATP TIRF transients are due to binding of Alexa-ATP to the active site of HMM is clear from their disappearance when the active site is blocked by regular ATP (Supporting Information Figure 4). Moreover, in contrast to the difference between TMCS and SiO₂, an increase in temperature from 15 to 25 °C increased the rate constants of all exponential processes by a factor between 1.35 and 1.91 in agreement with $Q_{10} < 2$ for the myosin ATPase.⁵⁴ This supports the view that all exponential phases are attributed to the rate limiting step of the Alexa-ATP turnover at the myosin active site. High-pressure liquid chromatography based ATPase assays giving similar overall ATPase activity as deduced from the TIRF based assays (Supporting Information) lend further support to this idea. The three exponential processes in the decaying TIRF transient are likely to be attributed to HMM configurations with different catalytic activity.³³ Whereas myosin heads that are tethered to the surface are expected to exhibit low activity^{33,55,56} heads several nm away from the surface are likely to have an catalytic activity similar to that in solution.⁵⁶

Geometry of HMM Adsorption on TMCS. The experimental results (particularly the FLIC data) show that a majority of the S1 units of HMM are too far from the TMCS surface to allow adsorption via head and neck regions. The 150 amino acids⁵⁷ C-terminal “hinge-region” of HMM, preserved in preparation of HMM under our conditions (*cf.* refs 58 and 59), is therefore the only reasonable candidate for adsorption to TMCS. This idea is consistent with its considerably lower stability than the rest of the S2-unit, opening for adsorption driven by gain in conformational entropy and hydrophobic effects.^{4,36,57,60–63} This would result in a HMM configuration as in Figure 5A, similar to the proposed actin propelling configuration on nitrocellulose.⁵⁹ Predominant one-point adsorption at the C-terminal accords

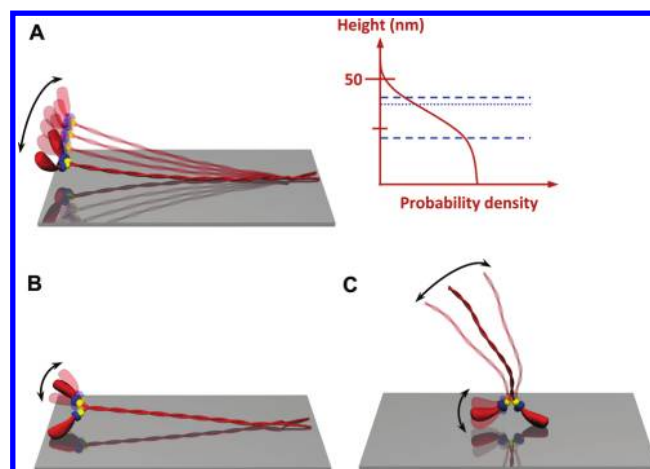


Figure 5. Model with proposed HMM configurations on negatively charged surfaces of different hydrophobicity and charge density. (A) Configuration believed to dominate on TMCS. A tentative probability density distribution (based on QCM-D, FLIC studies, and theoretical considerations) for the position of the myosin head is illustrated to the right. Dashed lines indicate the heights obtained in two different QCM-D models and dotted line indicates height obtained in FLIC microscopy studies. The curved arrow indicates thermal fluctuations. (B) Geometry that may exist on both SiO₂ and TMCS to a minor degree. (C) Geometry believed to dominate on negatively charged hydrophilic SiO₂.

with the general finding of preferential end-on adsorption of elongated proteins at high surface coverage.³⁶ That C-terminal adsorption should lead to more extensive unfolding of the S2-unit,⁵ beyond the “hinge region”, cannot be excluded but seems less likely in view of higher stability of the S2-unit outside this region.^{57,60} Moreover, more extensive unfolding is difficult to reconcile with large height of the HMM layer in the QCM-D studies, the small HMM footprint and the findings that the catalytic sites and the actin binding sites are 20–30 and almost 40 nm, respectively above the surface.

If the link between the surface-adsorbed C-terminal hinge region and the coiled coil part of the tail exhibits similar flexibility as a coiled coil (persistence length 130 nm)⁴ the entire S2 region may be treated as a cantilevered beam. From equipartition of energy it follows that the neck-tail junction, on average (root-mean-square), would be 20 nm above the surface due to thermal fluctuations (Supporting Information). If the hinge region instead gives a flexible coupling to the surface, similar to that in myosin molecules incorporated into synthetic thick filaments,⁶³ the neck-tail junction would be expected to be, on average, 40 nm above the surface with the actin-binding region even further away. The height estimates for the HMM layer on TMCS (< 40 nm), based on FLIC and QCM-D data, fit best with a stiff surface attachment via the C-terminal tail.

(54) Bagshaw, C. R.; Trentham, D. R. *Biochem. J.* **1974**, *141*, 331–349.

(55) Hayashi, H.; Takiguchi, K.; Higashi-Fujime, S. *J. Biochem. (Tokyo)* **1989**, *105*, 875–877.

(56) Highsmith, S.; Duignan, K.; Franks-Skiba, K.; Polosukhina, K.; Cooke, R. *Biophys. J.* **1998**, *74*, 1465–1472.

(57) Lu, R. C.; Wong, A. *J. Biol. Chem.* **1985**, *260*, 3456–3461.

(58) Weeds, A. G.; Pope, B. *J. Mol. Biol.* **1977**, *111*, 129–157.

(59) Toyoshima, Y. *Adv. Exp. Med. Biol.* **1993**, *332*, 259–265.

(60) Lopez-Lacomba, J. L.; Guzman, M.; Cortijo, M.; Mateo, P. L.; Aguirre, R.; Harvey, S. C.; Cheung, H. C. *Biopolymers* **1989**, *28*, 2143–2159.

(61) Lu, R. C. *Proc. Natl. Acad. Sci.-Biol.* **1980**, *77*, 2010–2013.

(62) Walker, M.; Trinick, J. *J. Mol. Biol.* **1986**, *192*, 661–667.

(63) Gundapaneni, D.; Xu, J.; Root, D. D. *J. Struct. Biol.* **2005**, *149*, 117–126.

It is self-evident, from the above, that immobilization of the HMM molecules only at their C-terminal should give rise to a highly dynamic HMM layer with an expected mass density distribution approximately indicated in Figure 5A. From the persistence length of a coiled-coil, first passage times $< 100 \mu\text{s}$ are expected for the neck-tail junction to reach 50 nm above the surface (cf. refs 25 and 64 and the Supporting Information). However, at each given point in time a very low fraction of the heads is that far above the surface.

The TIRF Alexa-ATP studies suggest that a fraction of the HMM heads ($\sim 16\%$; corresponding to slow exponential processes A_2 and A_3) on TMCS may also be immobilized on the surface with a side-on configuration of the HMM molecule (Figure 5B). Such geometries in hydrated conditions prior to fixation for electron microscopy have been suggested to account for the appearance of a substantial fraction of the HMM molecules in electronmicrographs.⁶⁵ Related configurations on nitrocellulose have also been proposed,⁵⁹ but side-on configurations are likely to be more frequent at low HMM density.^{4,36}

Geometry of HMM Adsorption on SiO_2 . Limited or no actin binding and lack of motility on SiO_2 show that only few HMM molecules are available to interact with actin on this surface. This fits with the idea that a majority of the HMM molecules adsorb to SiO_2 via their head parts^{4,9,14} (Figure 5C), consistent with the increased fraction of slow Alexa-ATP decay phases (Figure 4B) and a dominating fraction of the catalytic sites very close to the SiO_2 surface (Figure 2C).

For a dense HMM layer, surface adsorption only via the actin binding region rather than via both this region and the C-terminal hinge³⁶ is most likely, causing the tails to extend a substantial distance into the solution. This idea accounts for the large heights in the QCM-D data and is consistent with expected repulsion between the HMM tails and between the tails and the SiO_2 surface.⁶⁶ The FLIC studies suggest actin binding by HMM > 80 nm above the SiO_2 surface. The substantially larger height than in the QCM-D study, the limited actin binding even in the absence of ATP and the finding that a majority of the HMM catalytic sites are close to the surface on SiO_2 suggests that the actin binding is due to a very small fraction of the HMM molecules. This is also supported by the similar average head heights on TMCS and SiO_2 (within ± 15 nm) in the FLIC studies in Figure 2C and the TIRF studies in Figure 3. Moreover, since a height of 100 nm is incompatible with the HMM length, there must be a very sparse second HMM layer where the molecules adsorb via their C-terminal tail regions to the tail regions of HMM molecules like those in Figures 5C and 2E. This idea is consistent with observations⁶⁷ of self-association between long S2 particles via their hinge regions.

The fractional amplitude of slow phases in the Alexa-ATP TIRF transients (A_2 and A_3) amounted to only 36% whereas the FLIC data suggest that a vast majority (99%) of the catalytic sites are within approximately 5 nm from the SiO_2 surface. These results could be accounted for if all heads that are immobilized on SiO_2 do not exhibit a reduced ATP turnover rate. Alternatively, the TIRF spectroscopy results, but not the FLIC data (using other optics), might underestimate the fluorescence intensity attributed to Alexa-nucleotide close to the surface. Other ideas

to, at least partly, explain the discrepancy between the TIRF-ATPase and FLIC data with Alexa-ATP would be that only one of the heads of slightly more than 70% of the HMM molecules adsorbs strongly (cf.;⁶⁵ Figure 5C) on SiO_2 . This would be consistent with the two slow phases in the TIRF-ATPase data amounting to only 36% but with 72% of the heads close to the surface. A small fraction of the HMM molecules may also adsorb via the C-terminal tail region (Figure 5B) since the structural instability of this region would open for adsorption also on charged hydrophilic surfaces.³⁶

Importantly, none of the free heads in the configurations in Figure 5A–C would be available for actin binding on SiO_2 since the tails in the configuration in Figure 5C extend further out than the heads. The tails are negatively charged, like actin and their persistence length of 130 nm (almost 3 times their length) suggest that they would not buckle appreciably due to thermal collisions. Thus, a “forest” of closely spaced HMM tails, would effectively hinder the actin filaments from reaching the free myosin heads.

Geometry of HMM Adsorption on Negatively Charged Surfaces of Different Hydrophobicities. It was found⁹ that increased contact angle from 20° for piranha cleaned glass to 70° for a silanized glass/ SiO_2 surface was associated with reduced negative surface charge density (according to zeta potential measurements) by 50%. Since the present data represent the extreme contact angles and surface charge densities in the previous study,⁹ the velocity data for the range of contact angles in that work can presumably be accommodated by a contact angle dependence of the proportion of the different HMM configurations in Figure 5. Thus, with increased contact angle the surface adsorption via the C-terminal hinge region of actin propelling HMM molecules is likely to increase. Simultaneously the tendency for electrostatic adsorption via the positively charged actin binding loops of HMM^{4,22} would be reduced.

In the case with high surface coverage and relatively high HMM incubation concentration the HMM molecules in solution would preferentially approach the surface in the end-on configuration,⁴ *a priori* with equal probability for the actin binding and C-terminal hinge region. The probability that adsorption occurs upon a given approach would be determined by the surface properties as described above. Unlike the situation at high HMM incubation concentrations (as in the present work), initial adsorption via one region of the HMM molecule at low HMM incubation concentrations would give rise to repeated hits between the free HMM end and the surface, increasing the probability for two-point adsorption as seen with other elongated proteins.³⁶ A similar situation may also apply to the first adsorbing HMM molecules at high incubation concentrations, consistent with the idea that there is a fraction of heads with two-point adsorption also in the present study (see also refs 5 and 59).

Implications for Fundamental Studies and Nanotechnological Applications. There are several small differences between actomyosin interactions in the IVMA and in the ordered myofilament lattice of muscle that may cause more or less subtle inconsistencies between experimental results in the two systems.⁴ The large surface–actin distance in the IVMA that we observe here should also be considered in this connection. This large distance and substantial thermal fluctuations of the HMM molecules is also of interest in relation to other observations. For instance, it has been assumed that HMM molecules at lower surface coverage may reach and bind to actin filaments more than 20 nm away from their surface attachment point. This idea is generally consistent with the present results. Thus, if the S1–S2 junction is, on average, 20 nm above the surface due to thermal motion it is also expected to move over a range with standard

(64) Howard, J. *Mechanics of motor proteins and the cytoskeleton*; Sinauer Associates Inc: Sunderland, MA, 2001.

(65) Offer, G.; Knight, P. J. *Mol. Biol.* **1996**, *256*, 407–416.

(66) Albet-Torres, N.; Bloemink, M. J.; Barman, T.; Candau, R.; Frölander, K.; Geeves, M. A.; Golker, K.; Herrmann, C.; Lionne, C.; Piperio, C.; Schmitz, S.; Veigel, C.; Månsson, A. *J. Biol. Chem.* **2009**, *284*, 22926–22937.

(67) Sutoh, K.; Karr, T.; Harrington, W. F. *J. Mol. Biol.* **1978**, *126*, 1–22.

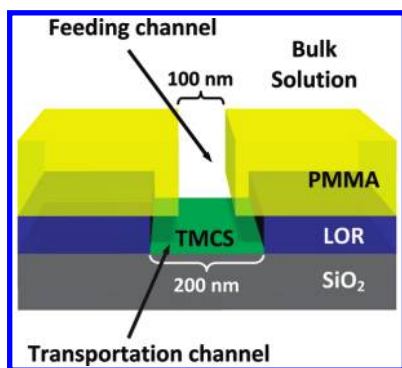


Figure 6. Schematic drawing of inverted T cross-sectional profile of bilayer resist channels produced by electron-beam lithography and subsequent etching of the lift-off resist (LOR).²¹ Before incubation with HMM, the poly methyl methacrylate (PMMA) layer was made hydrophilic and negatively charged by oxygen plasma treatment. The dimensions of the inverted T-channel are similar to those in refs 21, 25, and 26, giving excellent guidance and unidirectional HMM propelled actin filament sliding.

deviation of ± 20 nm in the horizontal plane. This is in reasonable agreement with a bandwidth of 30 nm used by Uyeda et al.⁶⁸ based on electron microscopic observations.

It has been shown that inverted T-profile channels (Figure 6) intended to guide HMM induced transportation of actin-attached cargoes in lab-on-a-chip devices should have a width < 200 nm to ensure unidirectional actin filament sliding.^{21,25} This is a similar order of magnitude as the thickness of the HMM layers found here. The optimal functionality of the channels may therefore depend critically on the exact channel dimensions.^{21,25} If the floor of the inverted T-channels is coated with TMCS, the HMM layer thickness would be 40 nm. The feeding-channel (vertical part of inverted T-profile), for communication between the transportation channel (Figure 6) and the bulk fluid has, in current implementations, been surrounded by hydrophilic, negatively charged poly(methyl methacrylate) (PMMA).^{14,25} In view of the chemical properties, one would expect that this PMMA surface is covered with HMM molecules with tails extending at least 50 nm from the surface. Thus, soon after HMM incubation, the feeding channels (total width about 100 nm) are likely to be almost completely clogged with HMM molecules. This would compromise the filling of the transportation channels with HMM. The observation of effective HMM propelled actin filament sliding with even narrower feeding channels,²¹ may be explained if clogged feeding channels prevent escape of actin filaments

allowing actin transportation at quite low HMM density on the TMCS floor. Another complication for lab-on-a-chip devices, with the design in Figure 6, is that the relatively large HMM layer heights on both TMCS and PMMA may limit the free space in the transportation channels. This is important to consider in the design of the channels to allow transportation of reasonably bulky cargoes.

It has been demonstrated with kinesin propelled microtubules that cargoes may be picked up from localized surface patches^{27,28} by motor propelled cytoskeletal filaments. Alternatively, such patches may be loaded with recognition molecules for capturing motor transported analytes (microorganisms, proteins) in diagnostics (cf. ref 69). The present work shows that implementation of such applications using actomyosin will require that the recognition molecules or intended cargoes are placed on pedestals, raised sufficiently above the surface, to reach the HMM propelled actin filaments.

Acknowledgment. The work was supported by The Swedish Research Council (Project No. 621-2007-6137), The Carl Trygger Foundation, The Crafoord Foundation, The Magnus Bergvall Foundation, The Helge Ax:son Johnson Foundation, Sparbanksstiftelsen Kronan, and The Faculty of Natural Sciences and Engineering, University of Kalmar and Linnaeus University. Discussions with Professor Sven Tågerud are gratefully acknowledged.

Supporting Information Available: Text giving details of experiments and analyses, surface characterization with respect to contact angle and motor function, TIRF spectroscopy studies of HMM adsorption, Alexa-ATP fluorescence intensity, steady-state hydrolysis of Alexa-ATP by HMM on surfaces and in solution, HMM compared to myosin subfragment 1 in TIRF studies, TIRF experiments with HMM from *M. psoas major* and theoretical considerations related to thermal fluctuations of surface-adsorbed HMM, with figures showing characterization of myosin, HMM and S1 preparations by SDS-PAGE, a schematic illustration of key techniques, fluorescence spectroscopy measurements of HMM, Alexa-ATP TIRF transients under special conditions, and comparative studies showing total internal reflection (TIRF) fluorescence transients based on surface-adsorbed HMM and S1 and tables of results of triple exponential fits to decaying phase of Alexa-ATP TIRF transient. This material is available free of charge via the Internet at <http://pubs.acs.org>.

(68) Uyeda, T. Q.; Kron, S. J.; Spudich, J. A. *J. Mol. Biol.* **1990**, *214*, 699–710.

(69) Fischer, T.; Agarwal, A.; Hess, H. *Nat. Nanotechnol.* **2009**, *4*, 162–166.